## **Supplementary information**

# Characterization of a High Detection-Sensitivity Atmospheric Pressure Interface Time-of-Flight Mass Spectrometer

Fabian Schmidt-Ott<sup>1,2</sup>, Somnath Bhowmick<sup>1</sup>, Alexandros Lekkas,<sup>3</sup> Dimitris Papanastasiou<sup>3</sup>, Anne Maisser<sup>1</sup>, George Biskos<sup>1,4</sup>

*Corresponding authors*: Fabian Schmidt-Ott (f.schmidt-ott@cyi.ac.cy) or George Biskos (g.biskos@cyi.ac.cy or g.biskos@tudelft.nl)

## S.1 Timing for accelerating ions into the TOF

Once released from the ion trap, ions travel approximately 0.5 m before reaching the orthogonal acceleration (OA) stage, where ion packets are injected into the TOF chamber in synchronization with their release. Because ions require a finite time to reach the OA stage, a delay occurs between their release from the trap and their orthogonal acceleration.

Furthermore, the delay is mass-dependent: larger ions take longer to travel from the ion trap exit to the OA stage and thus experience greater delays than smaller ions. This mass dependency in delay arises from the same principle that governs ion separation in the TOF chamber - larger ions experience lower acceleration across an electric field and therefore travel at lower velocities. Accurate synchronization of ion release from the trap with the OA pulsing is therefore essential to prevent ion losses due to mismatched timing.

To characterize this mass-dependent delay, transmission was measured using ion samples with distinctly different masses (see Fig. S-1). An ion of 74 Da showed optimal transmission with a 40  $\mu$ s delay, whereas an ion of 690 Da required a 110  $\mu$ s delay. Based on these results, the OA delays summarized in Table 1 were selected, with shorter delays applied to the low-mass range and longer delays to the high-mass range.

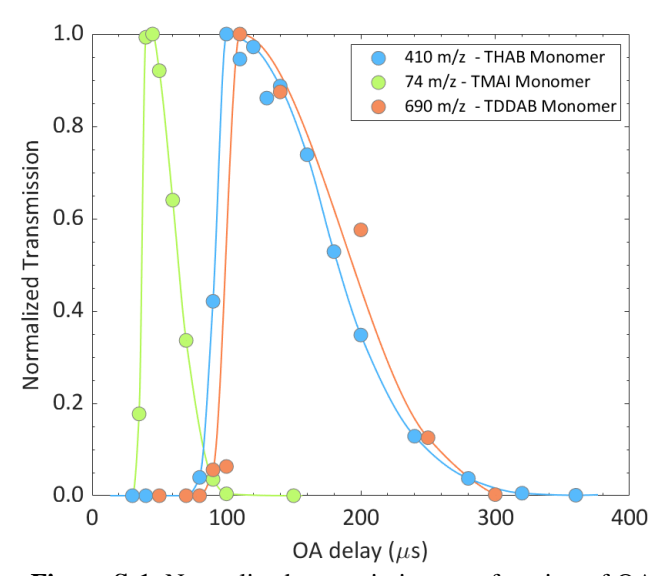


**Figure S-1.** Normalized transmission as a function of OA timing. The transmission was normalized with respect to the highest value, because the transmission was different for each ion standard.

<sup>&</sup>lt;sup>1</sup> Climate and Atmosphere Research Centre, The Cyprus Institute, 2121 Nicosia, Cyprus

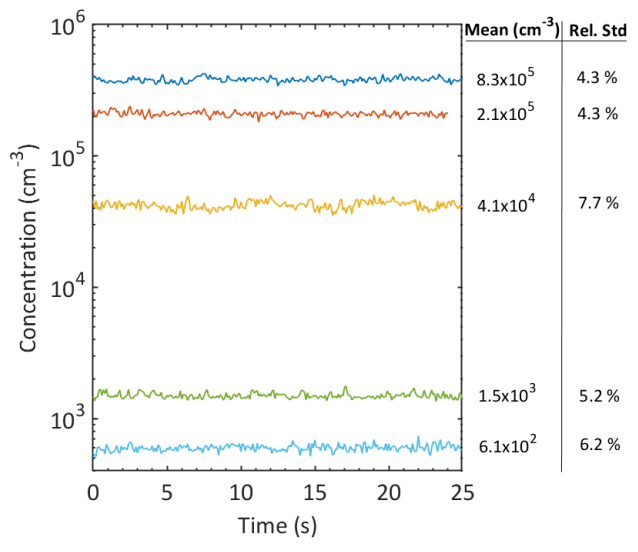
<sup>&</sup>lt;sup>2</sup> Institute for Atmospheric and Earth System Research, University of Helsinki, 00014, Helsinki, Finland

<sup>&</sup>lt;sup>3</sup> Fasmatech Science and Technology SA, TESPA Lefkippos, NCSR Demokritos, 15310 Athens, Greece

<sup>&</sup>lt;sup>4</sup> Faculty of Civil Engineering and Geosciences, Delft University of Technology, 2628 CN, Delft, The Netherlands

## S.2 Ion production stability

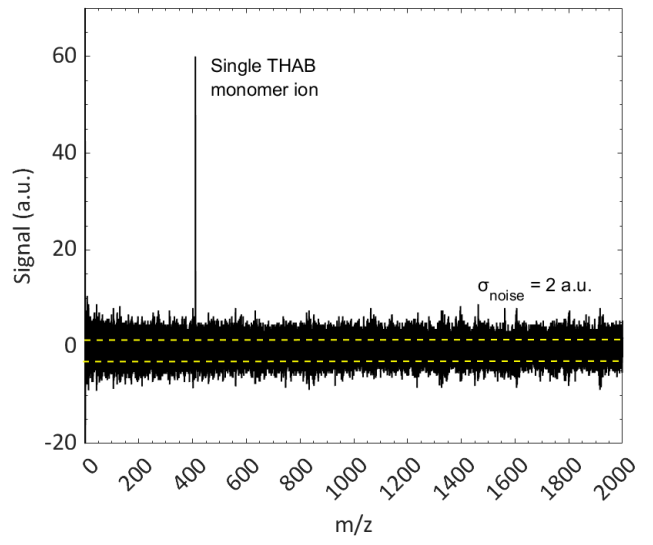
Figure S-2 shows the temporal variation of the THAB concentration produced by electrospray. Since all measurements required a stable source of ions, we ensured that the relative standard deviation was approximately 10% or less in all cases.



**Figure S-2.** Stability of THAB monomer production when electrosprayed at different concentrations.

## S.3 Single-ion measurements

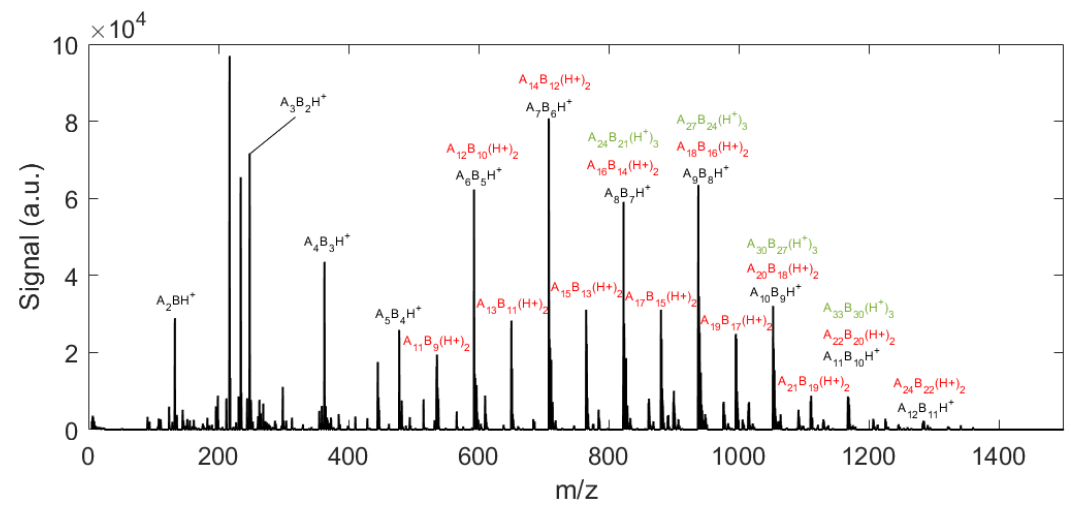
The lowest possible signal that the TOF detector (i.e., a MagneTOF® detector) of the APi-TOF MS can measure is that of a single ion striking the detector ( $S_{ion}$ ; Simke et al., 2024). As indicated by the recorded spectrum shown in Figure S-3, this signal is 60 a.u. and lies well above the noise level of the detector that has a standard deviation ( $\sigma_{noise}$ ) of 2 a.u. Consequently, the SNR (which is equal to  $S_{ion}/\sigma_{noise}$ ) corresponding to the single-ion peak is approximately 30, which is line with the recommended minimum threshold of 10 (Gross, 2006). We should note here that the value of  $S_{ion}$  is used to determine the count rate and from that the transmission of the APi-TOF-MS system by Eq. 1 in the main manuscript.



**Figure S-3.** A single non-averaged mass spectrum showing the signal induced by a single THAB monomer striking the TOF detector.

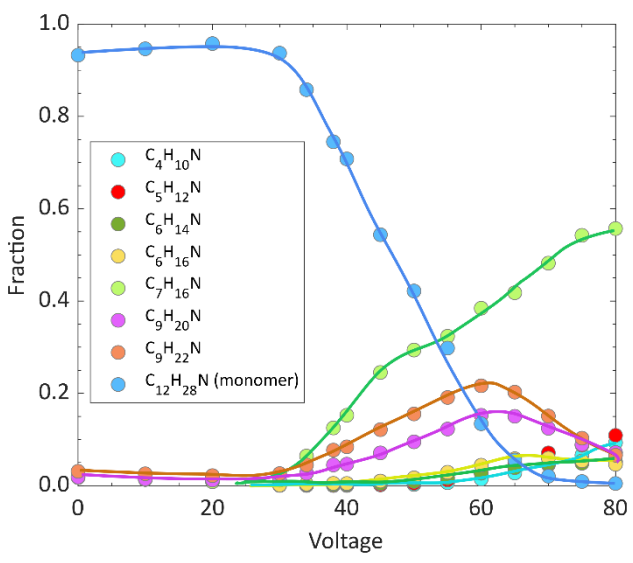
## S.4 Sulphuric acid – amine clusters

Figure S-4 shows the mass spectrum of ionic clusters comprised of amine (NH<sub>3</sub>) and sulphuric acid (H<sub>2</sub>SO<sub>4</sub>), with the general formulation (NH<sub>3</sub>)<sub>x</sub>(H<sub>2</sub>SO<sub>4</sub>)<sub>x-y</sub>(H<sup>+</sup>)<sub>y</sub>. These clusters were produced by electrospraying a solution of ammonium sulphate in methanol as described by Waller et al. (2019).



**Figure S-4.** Amine – sulphuric acid clusters generated by electrospraying an ammonium sulphate methanol solution. Key: A stands for  $NH_3$ . and B for  $H_2SO_4$ .

Figure S-5 shows the CID as the TPAI monomer brakes into its fragments at varying voltages across the funnel and ion trap, corresponding to different kinetic energies. For this measurement, only the TPAI monomer was selected by the DMA upstream the APi-TOF-MS system. Fragmentation onset here is at 25 V, which is lower than the onset observed for the TPAI monomer when the dimer is present, which occurs at 45 V, as shown in Figure 6 in the main manuscript. Apparently, the dimer breaks first, before the molecule itself can fragment in smaller pieces. This is consistent with the fact that ionic bonds holding the dimer together are generally weaker than covalent bondings within the monomer molecules.



**Figure S-5.** Collision-induced dissociation of TPAI monomers at different voltages across the funnel and ion trap, shown as the fraction of the species with respect to the total ion signal. The monomer concentration introduced to the API-TOF MS is  $5 \times 10^4$  ions/cm<sup>3</sup>.

## S.5 TPAI and THAB dimer stability

We used the ABCluster programme in combination with the Gaussian 16 *ab initio* electronic structure calculation package to determine ground state equilibrium geometries of THAB and TPAI monomers and dimers (Frisch et al., 2019; Zhang & Dolg, 2015). ABCluster employs the artificial bee colony algorithm to efficiently explore the potential energy surface of a molecular system. The structures obtained from ABCluster were then fully optimized using density functional theory (DFT) with the ωB97X-D [7] hybrid functional and Def2-TZVP basis set [8] to identify ground state equilibrium geometries of THAB and TPAI monomers and dimers (Chai & Head-Gordon, 2008; Jones, 2015; Weigend & Ahlrichs, 2005). Similar computational approaches have been shown to reproduce molecular geometries and electronic properties in close agreement with the experimental results for similar systems (Domingos et al., 2021).

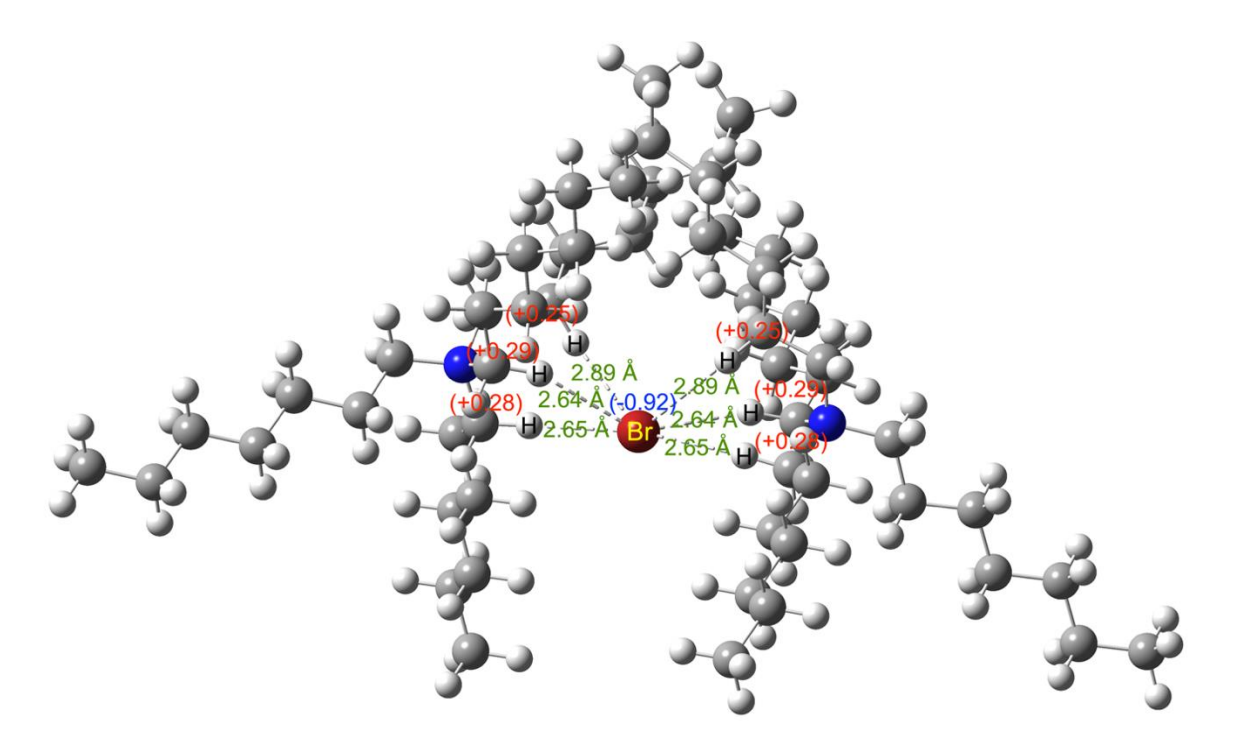


**Figure S-6.** Optimized equilibrium geometry of the THAB dimer calculated at the  $\omega B97X$ -D/def2-TZVP level of theory. Atoms participating in the hydrogen bond (Br and H) are labeled, with partial atomic charges indicated in brackets. The hydrogen bond is depicted as a dashed line, and the corresponding interatomic distance (in Å) is shown in green.

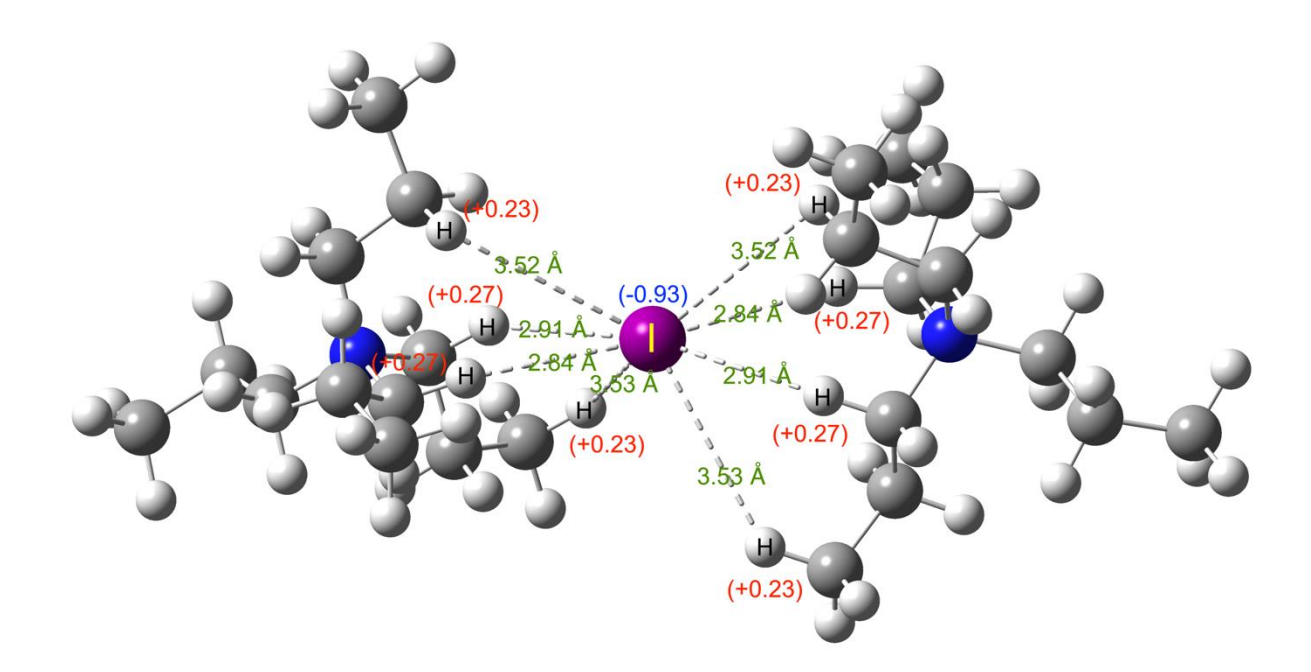


**Figure S-7.** Optimized equilibrium geometry of the TPAI dimer calculated at the  $\omega$ B97X-D/def2-TZVP level of theory. Atoms participating in the hydrogen bond (I and H) are labeled, with partial atomic charges indicated in brackets. The hydrogen bond is depicted as a dashed line, and the corresponding interatomic distance (in Å) is shown in green.

The optimized geometries of THAB and TPAI dimers are illustrated in Figures S1 and S2. In both systems, the most dominating stabilizing interactions between the two monomer units are hydrogen bonds between the halogen atom (Br or I) and the hydrogen atoms of the monomers. The presence and nature of these hydrogen bonds were confirmed by Quantum Theory of Atoms in Molecules analysis performed using the Multiwfn program (Lu & Chen, 2012; Richard & Bader, 1990). Partial atomic charges on the atoms involved in these hydrogen bonds were obtained using the Natural Population Analysis method, and the values for the H and halogen atoms were found to be similar in both dimers (Reed et al., 1985).

Structurally, the TPAI dimer contains eight hydrogen bonds compared to six in the THAB dimer. However, the average hydrogen bond length in the TPAI dimer is longer. Specifically, in the TPAI dimer, two hydrogen bonds are very long (3.52 Å) and four others fall in the range of 2.84-2.91 Å. In contrast, in the THAB dimer, four hydrogen bonds are significantly shorter ( $\approx$ 2.65 Å), and the remaining two are slightly longer ( $\approx$ 2.89 Å). This trend suggests that the hydrogen bonds in TPAI dimer are generally weaker than those in the THAB dimer. The above statement is supported by the quantitative estimation of hydrogen bond strength obtained from Espinosa's relation (Espinosa et al., 1998). For the THAB dimer, the hydrogen bond energies range from 1.55 to 2.15 kcal/mol, whereas for the TPAI dimer, they range from 0.52 to 1.71 kcal/mol. When expressed as the average hydrogen bond energy per bond, the THAB dimer exhibits a significantly higher value (1.94 kcal/mol) compared to TPAI dimer (1.13 kcal/mol).

An alternative approach to evaluate the relative stability of the THAB and TPAI dimers is to compare their total energies with those of their dissociated products. In APi-TOF-MS, collision-induced dissociation of both dimers yields the product sets shown in reaction paths 1 and 2 shown in Figure S-8 below.

$$(C_{28}H_{60}N)_2Br^+ \begin{cases} (C_{28}H_{60}N)^+ + (C_{28}H_{60}N)Br & (1a) & \Delta E = 40.04 \ kcal/mol \\ \\ 2(C_{28}H_{60}N)^+ + Br^- & (1b) & \Delta E = 122.20 \ kcal/mol \\ \\ (C_{12}H_{28}N)_2I^+ \end{cases}$$
 
$$(C_{12}H_{28}N)^+ + (C_{12}H_{28}N)I \qquad (2a) \qquad \Delta E = 31.14 \ kcal/mol \\ \\ (C_{12}H_{28}N)^+ + I^- \qquad (2b) \qquad \Delta E = 111.45 \ kcal/mol \\ \end{cases}$$

 $\Delta E$  = sum of energies of the dissociated products – energy of the dimer

**Figure S-8.** Dissociation channels of THAB and TPAI dimers with associated stabilization energy values ( $\Delta E$ ).

If the total energy of the intact dimer (left-hand side of reaction paths 1 and 2) is lower than the sum of the energies of its dissociation products (right-hand side of the reaction paths), the dimer is considered stable with respect to dissociation. The stabilization energy,  $\Delta E$ , reported in Figure S-8, is the energy difference between the sum of energies of the products and intact dimer, and therefore, provides a direct measure of this stability; i.e., larger and positive  $\Delta E$  values correspond to greater overall stability.

DFT calculations show that  $\Delta E$  is positive for all dissociation channels of both dimers, consistent with their behavior in our APi-TOF-MS system. For a particular dissociation channel, the  $\Delta E$  values for the THAB dimer are 9 to 11 kcal/mol larger than those for the TPAI dimer, indicating greater stability. The enhanced stability allows the THAB dimer to resist higher collisional energies before dissociating, whereas the weaker hydrogen bonding and lower  $\Delta E$  values in the TPAI dimer make it more prone to fragmentation. As a result, TPAI dimers dissociate at lower collision energies in APi-TOF-MS measurements, which is in agreement with our experimental observation.

#### References

- Chai, J.-D., & Head-Gordon, M. (2008). Long-range corrected hybrid density functionals with damped atom—atom dispersion corrections. *Physical Chemistry Chemical Physics*, 10(44), 6615. https://doi.org/10.1039/b810189b
- Domingos, S. R., Pérez, C., Kreienborg, N. M., Merten, C., & Schnell, M. (2021). Dynamic chiral self-recognition in aromatic dimers of styrene oxide revealed by rotational spectroscopy. *Communications Chemistry*, *4*(1), 32. https://doi.org/10.1038/s42004-021-00468-4
- Espinosa, E., Molins, E., & Lecomte, C. (1998). Hydrogen bond strengths revealed by topological analyses of experimentally observed electron densities. *Chemical Physics Letters*, 285(3–4), 170–173. https://doi.org/10.1016/S0009-2614(98)00036-0
- Gaussian 16, Revision C.01, Frisch, M. J.; Trucks, G. W.; Schlegel, H. B.; Scuseria, G. E.; Robb, M. A.; Cheeseman, J. R.; Scalmani, G.; Barone, V.; Petersson, G. A.; Nakatsuji, H.; Li, X.; Caricato, M.; Marenich, A. V.; Bloino, J.; Janesko, B. G.; Gomperts, R.; Mennucci, B.; Hratchian, H. P.; Ortiz, J. V.; Izmaylov, A. F.; Sonnenberg, J. L.; Williams-Young, D.; Ding, F.; Lipparini, F.; Egidi, F.; Goings, J.; Peng, B.; Petrone, A.; Henderson, T.; Ranasinghe, D.; Zakrzewski, V. G.; Gao, J.; Rega, N.; Zheng, G.; Liang, W.; Hada, M.; Ehara, M.; Toyota, K.; Fukuda, R.; Hasegawa, J.; Ishida, M.; Nakajima, T.; Honda, Y.; Kitao, O.; Nakai, H.; Vreven, T.; Throssell, K.; Montgomery, J. A., Jr.; Peralta, J. E.; Ogliaro, F.; Bearpark, M. J.; Heyd, J. J.; Brothers, E. N.; Kudin, K. N.; Staroverov, V. N.; Keith, T. A.; Kobayashi, R.; Normand, J.; Raghavachari, K.; Rendell, A. P.; Burant, J. C.; Iyengar, S. S.; Tomasi, J.; Cossi, M.; Millam, J. M.; Klene, M.; Adamo, C.; Cammi, R.; Ochterski, J. W.; Martin, R. L.;

- Morokuma, K.; Farkas, O.; Foresman, J. B.; Fox, D. J. (2016) Gaussian, Inc., Wallingford CT.Gross, J. H. (2006). *Mass spectrometry: A textbook*. Springer Science & Business Media.
- Jones, R. O. (2015). Density functional theory: Its origins, rise to prominence, and future. *Reviews of Modern Physics*, 87(3), 897–923. https://doi.org/10.1103/RevModPhys.87.897
- Lu, T., & Chen, F. (2012). Multiwfn: A multifunctional wavefunction analyzer. *Journal of Computational Chemistry*, *33*(5), 580–592. https://doi.org/10.1002/jcc.22885
- Reed, A. E., Weinstock, R. B., & Weinhold, F. (1985). Natural population analysis. *The Journal of Chemical Physics*, 83(2), 735–746. https://doi.org/10.1063/1.449486
- Richard, F., & Bader, R. (1990). Atoms in molecules: A quantum theory.
- Simke, F., Fischer, P., & Schweikhard, L. (2024). Evaluation of MagneTOF detector signals for the determination of many-ion bunches. *International Journal of Mass Spectrometry*, *506*, 117337. https://doi.org/10.1016/j.ijms.2024.117337
- Waller, S. E., Yang, Y., Castracane, E., Kreinbihl, J. J., Nickson, K. A., & Johnson, C. J. (2019). Electrospray Ionization–Based Synthesis and Validation of Amine-Sulfuric Acid Clusters of Relevance to Atmospheric New Particle Formation. *Journal of the American Society for Mass Spectrometry*, 30(11), 2267–2277. https://doi.org/10.1007/s13361-019-02322-3
- Weigend, F., & Ahlrichs, R. (2005). Balanced basis sets of split valence, triple zeta valence and quadruple zeta valence quality for H to Rn: Design and assessment of accuracy. *Physical Chemistry Chemical Physics*, 7(18), 3297. https://doi.org/10.1039/b508541a
- Zhang, J., & Dolg, M. (2015). ABCluster: The artificial bee colony algorithm for cluster global optimization. *Physical Chemistry Chemical Physics*, 17(37), 24173–24181. https://doi.org/10.1039/C5CP04060D